Nature Communications

https://doi.org/10.1038/s41467-026-71754-9

Article in Press

Uncovering complex phonon interactions in $Mg_3Bi_{2-x}Sb_x$: topology and avoided crossings

Received: 21 May 2025

Accepted: 24 March 2026

Cite this article as: Chen, L., Yin, Y., Lu, T. *et al.* Uncovering complex phonon interactions in $Mg_3Bi_{2-x}Sb_x$: topology and avoided crossings. *Nat Commun* (2026). https://doi.org/10.1038/s41467-026-71754-9

Lei Chen, Yuefeng Yin, Ting Lu, Huangshui Ma, Shuxian Zhang, Xinyue Zhang, Zhiwei Chen, Siqi Lin, Siqi Huo, Shengqing Xia, Richard A. Mole, Dehong Yu, Kirrily C. Rule, Weiyao Zhao, Julie Karel, Pingan Song, John Bell & Min Hong

Uncovering Complex Phonon Interactions in $Mg_3Bi_{2-x}Sb_x$: Topology and Avoided Crossings

Lei Chen[1, ^], Yuefeng Yin[2, ^], Ting Lu[1], Huangshui Ma[1], Shuxian Zhang[3], Xinyue Zhang[4], Zhiwei Chen[3], Siqi Lin[5], Siqi Huo[1], Shengqing Xia[6*], Richard A. Mole[7], Dehong Yu[7], Kirrily C. Rule[7], Weiyao Zhao[2*], Julie Karel[2], Pingan Song[1], John Bell[1], Min Hong[1*]

[1]*Centre for Future Materials and School of Science, Engineering and Digital Technologies, University of Southern Queensland, Springfield Central, QLD 4300, Australia*

[2] *Department of Materials Science & Engineering, Monash University, Clayton, Victoria 3800, Australia*

[3]*Interdisciplinary Materials Research Center, School of Materials Science and Engineering, Tongji University, Shanghai 201804, China*

[4]*School of Materials Science and Engineering, Shanghai University, Shanghai 200444, China*

[5]*College of Materials, Shanghai Dianji University, Shanghai 201306, China*

[6]*State Key Laboratory of Crystal Materials, Institute of Crystal Materials, Shandong University, Jinan, Shandong 250100, of China*

[7]*Australian Nuclear Science and Technology Organisation, Lucas Heights NSW 2234, Australia*

[^]*These authors contribute equally to this work: Lei Chen, Yuefeng Yin.*

**Corresponding author: shqxia@sdu.edu.cn, weiyao.zhao@monash.edu, min.hong@unisq.edu.au*

ABSTRACT

$Mg_3Bi_{2-x}Sb_x$ compounds have emerged as promising mid-temperature thermoelectric materials, due to their excellent electrical performance, and the ultralow thermal conductivity. In this study, we investigate the complex phonon interactions in $Mg_3Bi_{2-x}Sb_x$ compounds and reveal nontrivial symmetry-protected topological crossings and avoided-crossing phenomena in the phonon dispersion, arising from the strong coupling between the acoustic and low-energy optical phonons. By combining inelastic neutron scattering measurements with first-principles simulations, we identify robust band crossing protected by crystal symmetries and mode

inversion along the Γ - M direction in $Mg_3Bi_{2-x}Sb_x$ compounds, providing direct experimental evidence of topological phonons in a thermoelectric system. Furthermore, pronounced avoided crossings involving ultrasoft transverse acoustic modes are observed along the same direction, indicating significant hybridization with optical branches in the basal plane. The influence of Bi/Sb alloying on the phonon structure is also examined, revealing a broadened density of states (DOS) in the low- to mid-energy range for the Mg_3BiSb alloy. These findings establish $Mg_3Bi_{2-x}Sb_x$ compounds as a model system for studying symmetry-protected phonon topology and strong phonon-phonon interactions, offering new insights for lattice engineering in quantum and energy materials.

Introduction

The concept of topology has profoundly reshaped condensed matter physics by providing a framework for classifying and understanding exotic electronic states rooted in symmetry-protected degeneracies. Over the past two decades, this paradigm has led to the discovery of topological insulators,[1-3] Dirac and Weyl semimetals,[4] and nodal-line semimetals,[5,6] all of which exhibit unconventional transport and magnetic properties dictated by their nontrivial electronic band topology. Inspired by this progress, the concept of topological phonons (TPs), which are nontrivial topological features in phononic band structures, has emerged as a vibrant parallel field.[7,8] Just as band degeneracies and crossings in electronic systems give rise to novel phenomena, phonon band crossings protected by crystal symmetries are expected to profoundly influence lattice-mediated properties, including thermal conductivity, superconductivity, and structural stability.[9-12]

Theoretically, TPs have been predicted in a wide range of materials, manifesting as topological nodal-line phonons, Weyl phonons, topological edge/surface phonons, and higher-

order phonon states. [9,13,14] However, their experimental realization remains scarce, largely constrained by challenges in directly probing phonon band structures and resolving high-resolution dispersion relations, particularly under ambient or application-relevant conditions. Compared with the manipulation of topological electronic states in fermionic systems, controlling TPs is further complicated by the bosonic nature of phonons. Specifically, phonons fundamentally follow different statistical rules from electrons. Consequently, TP states cannot be tuned via carrier doping or electric field gating — strategies that are routinely employed to manipulate electronic topology.[15] This fundamental distinction renders the direct control or switching of phonon topology inherently difficult in experiments. A viable alternative is to leverage indirect control mechanism, such as electron-phonon coupling or magnetic field-phonon coupling, to engineer lattice dynamics. Recent studies have revealed that phonons can exhibit chiral-like behavior and respond to magnetic fields.[7,16,17] This opens up the possibility of manipulating phonons in certain materials by applying external magnetic fields, analogous to strategies used in electronic systems.

In this context, inelastic neutron and X-ray scattering (INS/IXS) techniques offer unique experimental advantages. As momentum-resolved probes, they enable direct mapping of phonon dispersion relations and can unambiguously reveal topological features, such as band crossings, avoided crossings, and symmetry-protected degeneracies. Although these methods do not directly “tune” phonon topology, they are the most powerful tools for detecting and verifying topological phonon states and their evolution under varying sample conditions (e.g., temperature, magnetic field or pressure), thereby addressing the observational challenges inherent to phonon topology. Notable progress includes the observation of double-Weyl phonons in FeSi and Dirac phonons in graphene, demonstrating the experimental feasibility of detecting TPs.[18,19] Nonetheless, experimental reports of TPs in functional materials such as

thermoelectrics (TEs) remain scarce, despite theoretical predictions that TPs could enhance phonon scattering and reduce lattice thermal conductivity (κ_L), thereby improving TE performance.[20-22] For example, density functional theory (DFT) predicts that in triple-point topological metals such as TaSb and TaBi, the coexistence of topological electronic bands and TP band crossings can yield high electronic mobility and significantly suppressed κ_L, respectively.[20] This combination positions such materials as promising "electronic-metal, phonon-glass" candidates, which is an ideal requirement for high-performance TEs.[20] Similarly, indirect evidence from $ZrTe_5$ suggests phonon softening near topological phase transitions, leading to enhanced phonon scattering and reduced κ_L.[21,22] These findings underscore the significant role of lattice dynamics mediated by TPs, particularly in promoting phonon-phonon scattering and achieving ultralow κ_L.

The performance of TE materials is quantified by the dimensionless figure of merit, defined as $zT = \frac{S^2\sigma}{\kappa}T$, where S is the Seebeck coefficient, σ is the electrical conductivity, and κ is the total thermal conductivity comprising both the electronic contribution (κ_e) and the lattice contribution (κ_L). Over the past decade, TE materials with intrinsically low κ_L, a parameter largely independent of and decoupled from electronic performance, have attracted considerable attention due to their excellent performance across a wide temperature range and their substantial potential for further enhancement.[23-25] For example, PbTe stands as one of the leading mid-temperature TE materials, exhibiting exceptionally low κ_L compared to other simple rock-salt compounds, alongside superior electrical properties. Delaire et al. employed inelastic neutron scattering (INS) combined with first-principles calculations to uncover the origin of the low κ_L in PbTe, revealing giant anharmonic phonon coupling among the transverse optical (TO), longitudinal acoustic (LA), and transverse acoustic (TA) phonon modes.[26]

Applying the same approach, Li et al. subsequently uncovered orbital-driven giant phonon anharmonicity in SnSe, another rising-star TE material characterized by extremely low κ_L and a *zT* exceeding 2.[27] Furthermore, the semiconductor compound $AgSbTe_2$ has attracted considerable interest for both TE and phase-change applications owing to its anomalously low, glass-like thermal conductivity ($\kappa_L \approx 0.7$ W m^{-1} K^{-1}), which is approximately three times lower than that of PbTe.[28] A combined INS and transmission electron microscopy (TEM) study by Ma et al. demonstrated that spontaneous nanostructuring is responsible for phonon scattering and the resulting suppression of κ_L.[29] More recently, Ren et al. identified the persistence of long-wavelength transverse acoustic phonons across the superionic transition of argyrodite Ag_8SnSe_6 and revealed a striking thermal broadening of low-energy phonons, providing evidence of extreme phonon anharmonicity and weak bonding, which are key factors responsible for the ultralow thermal conductivity (<0.5 W m^{-1} K^{-1}).[30] These studies collectively demonstrate that lattice dynamics, as revealed by INS, are central to understanding and engineering heat transport in TEs.

Recently, n-type $Mg_3Bi_{2-x}Sb_x$ compounds were reported to achieve TE performance comparable to that of commercial Bi_2Te_3 near ambient conditions, potentially at much lower cost and with better mechanical strength.[30-33] Extensive experimental and theoretical studies on the TE properties of $Mg_3Bi_{2-x}Sb_x$ compounds have led to impressive advances in optimizing electronic parameters. However, the origin of their intrinsically low κ_L, particularly from the perspective of lattice dynamics, remains incompletely understood. One of the most intriguing aspects of $Mg_3Bi_{2-x}Sb_x$ is its ability to achieve intrinsically low κ_L, despite its relatively low mass and simple crystal structure, especially when compared with conventional TE compounds such as PbTe or Bi_2Te_3.[34,35] Interestingly, when Mg is replaced by heavier elements such as Ca or Yb, κ_L increases anomalously, directly contradicting the expected suppression from increased

compositional complexity and heavier atomic mass.[36] Ding *et al*. reported a comprehensive analysis of phonons in the AMg_2X_2 series (*A* = Mg, Ca, and Yb; *X* = Bi and Sb) using INS and IXS combined with first-principles simulations. Their results reveal substantial phonon softening and flattening of low-energy TA phonons in Mg_3X_2 along the *c* axis compared to their ternary analogues. This behavior was traced to a specific Mg-*X* bond, which markedly enhances phonon scattering, enabling a threefold variation in κ_L within the Mg_3X_2 system.[37] Moreover, previous calculations indicate that Sb/Bi and *A*-site Mg are primarily responsible for low- and mid-frequency phonons respectively, which are the main heat carriers. Additionally, Mg_3Sb_2 and Mg_3Bi_2 share the same crystal structure (Fig. 1a) and exhibit comparable lattice parameters, and reduced κ_L can be achieved through Sb/Bi alloying. However, phonon propagation within the basal plane of ternary $Mg_3Bi_{2-x}Sb_x$ compounds remains poorly understood. More interestingly, recent reports have identified multiple TPs in the phonon bands of Mg_3Sb_2,[14] including a phonon band crossing between acoustic and optical modes in the basal plane along the Γ- *M* direction. These predicted TPs lie within the heat-carrying phonon energy range (below 10 meV) and may therefore contribute significantly to the suppression of κ_L. Notably, previous papers have reported nearly isotropic κ_L in the $Mg_3Bi_{2-x}Sb_x$ single crystals, which is contradictory with the expectation based on its anisotropic crystal strucure.[32,38] Ideally, the basal plane should bear significantly higher κ_L than the *c*-axis direction due to factors such as weak bonding between Mg (1) layers, soft shear modes, and highly anharmonic behaviour of acoustic phonons along the *c* axis.[36] The observed 'abnormally isotropic κ_L' thus suggests that additional factors governing in-plane phonon transport remain to be elucidated.

In this work, we present a combined experimental and theoretical study of phonons in $Mg_3Bi_{2-x}Sb_x$ using both time-of-flight (TOF) and triple-axis INS techniques, complemented by first-principles simulations based on DFT. Our results reveal symmetry-protected topological

crossings between longitudinal acoustic and optical phonons, including a mode inversion in $Mg_3Bi_{1.5}Sb_{0.5}$ single crystal along the Γ – M direction, representing a robust experimental observation of topological phonons in a TE material. Furthermore, we identify pronounced avoided-crossing behavior in the transverse acoustic branches along the same direction and a substantial broadening of the phonon density of states arising from Sb/Bi alloying. These features provide direct evidence for strong acoustic-optical mode interactions and support the hypothesis that nontrivial lattice dynamics, beyond simple considerations of atomic mass or bonding stiffness, govern the thermal transport in this system. Our findings establish $Mg_3Bi_{2-x}Sb_x$ as a platform for studying topological phonons in functional materials and suggest new design principles for TEs based on phonon band topology.

Results

Topological phonon band structure in $Mg_3Bi_{1.5}Sb_{0.5}$ single crystal

$Mg_3Bi_{2-x}Sb_x$ compounds crystallize in the $CaAl_2Si_2$-type structure (space group $\mathrm{P}\bar{3}m1$), as shown in Fig. 1a, characterized by alternating stacking of anionic $Mg_2Bi_{2-x}Sb_x$ slabs and Mg cation layers along the *c* axis. Our DFT simulations reveal three topological crossing points in $Mg_3Bi_{2-x}Sb_x$ near the Γ- M zone, one of which lies along Γ- M direction, as shown in Fig. 1b. The three-phonon process illustrated in Fig. 1c represents the intrinsic phonon-phonon scattering mechanism responsible for heat resistance, which can be enhanced by increasing the phonon-phonon scattering phase space and the number of available scattering channels. Here, the ω and q denote the phonon energy and momentum, respectively. Our INS results reveal two distinct types of interactions (or coupling) between acoustic and low-energy optical phonon bands along Γ- M for longitudinal and transverse phonons, respectively, as summarized in Fig. 1d. Specifically, these are the TP crossing and the avoided-crossing. The former has been

theoretically reported in various systems, while the latter has been observed in PbTe crystals, where it is driven by giant lattice anharmonicity and contributes to enhanced phonon scattering and reduced κ_L.[26] As indicated in Fig. 1d, the phonon dispersion measured by INS in this work is plotted with star symbols, revealing evidence of LA – optical phonon crossing along Γ- *M* (left panel), alongside an avoided crossing between TA and another optical phonon (right panel). These experiments and results are discussed in detail in the following section. Our DFT calculations further confirm the existence of TPs along Γ- *M* (Figs. S11-S13), and demonstrate their robustness against atomic disorder (Fig. S14).

DFT calculations were employed to compute the phonon spectrum and associated Grüneisen parameters in $Mg_3Bi_{2-x}Sb_x$. The results reveal TP structures across all compounds with varying Sb/Bi ratios and provide a more comprehensive understanding of how Sb/Bi alloying influences lattice dynamics, as illustrated in Fig. 2. First, no imaginary frequencies were observed in the calculated phonon dispersions for any of the alloy compositions, confirming their dynamical stability. Second, the degeneracies between acoustic and optical branches in the low-frequency region were preserved across all alloys, with a clear upshift in the degeneracy energy as the Sb concentration increased. Despite these similarities, subtle differences emerge when Bi and Sb atoms are mixed within the structure. The low-energy phonon dispersions of Mg_3Bi_2, encompassing both acoustic and optical modes, are softer than those of Mg_3Sb_2, corresponding to an increase in group velocity with increasing Sb content, as shown in Fig. S1. Additionally, anisotropic group velocities presented in Fig. S2 indicate that in-plane group velocities are substantially lower than those along the out-of-plane direction. The Grüneisen parameters of $Mg_3\ Bi_{2-x}Sb_x$ compounds exhibit large negative values, as illustrated in Fig. S3. Moreover, anisotropic analysis of the Grüneisen parameters in Fig. S4 reveals large negative values along

Γ - *M*, which may underlie the anharmonic phonon-phonon interactions discussed in the following section. Notably, both the group velocities and Grüneisen parameters of the Bi/Sb alloyed compounds show features close to those of Mg_3Bi_2 rather than Mg_3Sb_2, consistent with the experimental DOS results presented later. Spin-orbit coupling (SOC) is important for accurately assessing the electronic and phononic structures of topologically nontrivial compounds, especially those containing heavy elements such as bismuth. However, benchmark calculations including SOC for $Mg_3Bi_{1.5}Sb_{0.5}$ in this work yield phonon band structures that are qualitatively similar to those obtained without-SOC, aside from subtle frequency shifts, which is consistent with literature (Fig. S13).[39] In particular, the phonon band degeneracies at the acoustic - optical crossings remain preserved. Given that supercell phonon calculations with SOC are approximately an order of magnitude more computationally expensive those without SOC, the use of non-SOC calculations for the main results presented in Fig. 2 is well justified in this study.

Triple-axis inelastic neutron scattering experiments

We performed triple-axis INS experiments on a $Mg_3Bi_{1.5}Sb_{0.5}$ single crystal, aligned in the (HK0) scattering plane to access both Γ- *M* and Γ- *K* phonon modes, to verify the phonon dispersions, particularly the nontrivial topological modes in the basal plane predicted by simulations. Constant-*Q* scans for the longitudinal acoustic (LA) branch along the Γ - *M* direction were conducted at selected *Q*-vectors from the Brillouin zone (BZ) center Γ (2, 0, 0) to the zone boundary *M* (1.5, 0, 0), as shown in Fig. 3a. The scattering intensity as a function of energy transfer was fitted using a multi-Gaussian peak function (blue curves). At (1.9, 0, 0), close to the zone center, two Gaussian peaks centered at 3 ± 1 meV and 7.3 ± 0.4 meV are assigned to the LA and optical phonons, respectively. As the wavevector approaches the zone boundary, the LA

and optical phonons converge in energy and eventually merge into a single peak near (1.6, 0, 0), indicating a topological phonon band crossing between the two modes. Notably, at (1.65, 0, 0), the peak is significantly broadened, reflecting suppressed phonon lifetimes and enhanced anharmonic phonon-phonon scattering rates near the crossing region.[27] At the zone boundary, the LA and optical phonons separate again, with energies of ~ 4.7±0.4 meV and ~ 6.8±0.3 meV, respectively. Crucially, the lower-energy phonon retains an optical-like linewidth, while the higher-energy phonons exhibits LA-like characteristics, further confirming the band inversion between the LA and the optical modes. The extracted linewidths are plotted in the upper panels of Fig. 3e and 3f, revealing that the optical phonon linewidth is broader than that of the acoustic phonon. Analogous acoustic-optical phonon coupling has been previously reported in SnSe single crystals, where TO mode softens upon heating and merges with the TA mode near the BZ boundary.[27] This TA - TO coupling is associated with giant anharmonicity, leading to ultralow κ_L and outstanding TE performance in SnSe. In the present work, we observe LA - optical merging in $Mg_3Bi_{1.5}Sb_{0.5}$ arising from topological phonon band crossing. Based on simulations, we infer that this phonon band topology extends to all $Mg_3Bi_{2-x}Sb_x$ compounds and may contribute to the low κ_L in the basal plane through reduced phonon lifetimes. Unlike the simple phonon band folding observed in SnSe, the LA - optical crossing reported here is nontrivial, or topological in nature. Detailed DFT simulations are provided in the Supporting Information. Additionally, as clearly seen in Fig. 3e, the extracted energies of the first two measured LA points (blue stars) near the zone center are slightly lower than the DFT predicted values. However, within the TP crossing region, the measured energies of both LA and optical phonons (blue stars and red circles) show excellent agreement with the calculated dispersion. We attribute this discrepancy to the presence of two overlapping LA and optical modes. In this regime, the TP crossing gives rise to strong LA-optical interactions, resulting in substantially broadened

linewidths. Consequently, the experimental peak positions extracted from fitting represent an effective average of the two crossed contributions rather than the intrinsic energy of a single phonon mode.

The transverse acoustic (TA) phonons along Γ - *M*, however, exhibit distinctly different behavior, as shown in Fig. 3b. TA phonon measurements were conducted at several *Q* positions from the zone center (2, -1, 0) to the boundary (2, -0.5, 0) at 100 K. From the fitting results, the TA phonon peak at (2, -0.8, 0) is well resolved at 2.76±0.03 meV, well separated from the optical branch at 5.3±0.3 meV. As the wavevector moves toward the zone boundary, the TA phonon shifts to a slightly higher energy (3.22±0.04 meV) at (2, -0.7, 0) and then softens markedly near the zone boundary. The sharp line shape of the TA mode persists throughout this region, with a comparable linewidth of ~ 1 meV. Meanwhile, the optical mode remains at ~ 5.5 meV, with a typical linewidth of ~ 2 meV. It is also evident from Fig. 3f that, along the Γ - *M* direction, the measured optical branch agrees well with DFT calculations, whereas the TA mode exhibits pronounced softening. Such softening of the TA modes induced by the TO branches is considered evidence of strong anharmonic lattice dynamics. It should be noted that Taipan has an energy resolution of ~ 1 meV, which may affect the linewidth fitting of the TA phonon given its sharp profile. Moreover, the TA peak at (2, -0.9, 0) was not well-developed owing to the 'tailing effect' from the elastic line. In INS experiments, particularly near the BZ center (Γ point), a strong elastic peak (arising from Bragg diffraction with no energy transfer) is often present. Due to instrumental resolution broadening and imperfect sample crystallinity, this elastic peak is typically broadened rather than being a δ function, resulting in a long energy tail that extends into the low-energy inelastic region. This 'tailing effect' can obscure the detection of low-energy acoustic phonons, especially transverse acoustic modes close to the zone center, because the elastic scattering intensity is typically orders of magnitude higher than that of inelastic phonons,

as can be seen in Fig. 3a and b. To address this, we repeated the same scan on the high-resolution cold neutron spectrometer Sika (measured energy resolution of 0.13 meV), as shown in Fig. S5. The acoustic phonon peak close to Γ (2, -1, 0) is significantly better resolved in the Sika spectra due to the superior energy resolution, centered at 1.7±0.1 meV with a width of 0.9±0.1 meV. As *Q* moves toward the BZ boundary, the acoustic phonon peak energy increases slightly to 3.2±0.1 meV at (2, -0.7, 0) and then softens dramatically. The unexpected softening of TA phonons and the energy gap between the TA and optical modes are absent in DFT calculations, resembling the avoided-crossing effect observed in PbTe-SnTe compounds and can be attributed to anharmonic lattice dynamics.[26] These results provide valuable insight into and help explain the previously anisotropic κ_L.

Similar measurements were also conducted along the Γ - *K* directon, as shown in Fig. 3c and d. The LA phonon measurements were performed at several *Q* positions from the zone center (2, -1, 0) to the boundary (3, -1.5, 0), while the TA phonon measurements were carried out from the zone center (2, 0, 0) to the boundary (1.5, 1, 0) at 100 K. Acoustic phonon softening is observed in both the longitudinal and transverse branches. The observed anharmonic behavior of both longitudinal and transverse phonon modes in the basal plane in Fig. 3 points to a lattice-dynamical origin of the intrinsically ultralow κ_L in the $Mg_3Bi_{1.5}Sb_{0.5}$ compound. The peak positions and linewidths of the longitudinal and transverse phonons were extracted from the INS experimental results in Fig. 3a-d and are shown in the lower panels of Fig. 3e and f, along with the DFT-calculated phonon dispersions. It is evident that the linewidth of the optical phonons is broader than that of the acoustic phonons. Specifically, in the Γ - *M* region where the LA – optical phonon topological crossing occurs, a markedly broadened linewidth is observed, indicating strong anharmonic phonon-phonon interactions.

Temperature-dependent lattice dynamics of polycrystalline Mg_3BiSb

The phonon DOS spectra of the Bi/Sb alloy system are similar (Fig. S6), and can be grouped into low-, mid-, and high-energy phonons, as indicated by the colored boxes. Based on mode decomposition, Mg (2) contributes mainly to high-frequency phonons above 20 meV, whereas Mg (1) and Bi/Sb dominate the mid- and low-frequency regions, which are the primary heat carriers. To further investigate temperature dependence, we selected Mg_3BiSb, which has the same Bi and Sb content to balance their contributions, for time-of-flight INS experiments. The phonon DOS was measured on polycrystalline samples at various temperatures, using Pelican, the TOF - INS spectrometer at ANSTO. A detailed description of the measurements is provided in the Methods section. Fig. 4a shows the experimental generalized density of states (GDOS) of Mg_3BiSb at 300 K, compared with those of Mg_3Bi_2 and Mg_3Sb_2 from the literature.[37] All spectra in Fig. 4a were collected in neutron energy-gain mode, where the neutron gains energy from the sample, thus reflecting the phonon characteristics of the alloy system. The acoustic phonon cut-off for Mg_3Bi_2 and Mg_3BiSb is ~ 6 meV, lower than that of Mg_3Sb_2. Meanwhile, the mid-energy peak shifts to ~17 meV relative to those of Mg_3Bi_2 and Mg_3Sb_2. These features are reproduced in the DFT simulations shown in Fig. S6, demonstrating good agreement experiment and theory. In the 6-20 meV range, Mg_3BiSb exhibits a broader and flatter DOS curve resulting from the merging of DOS peaks of its binary counterparts, indicating broadened phonon bands arising from strong anharmonicity in this energy range. This anharmonicity enhances phonon-phonon scattering and thus contributes to the reduction of κ_L. The κ, κ_e and κ_L of the polycrystalline Mg_3Sb_2, Mg_3Bi_2 and Mg_3BiSb were measured and calculated using the Thermal Transport Option (TTO) on a Physical Properties Measurement System (PPMS, Quantum Design, Dynacool-14T) (Fig. S18). The κ_L of the Bi/Sb alloyed sample exhibits the lowest value, consistent with the DOS results presented here and previous literature.[40-43] The room-

temperature powder-averaged lattice dynamic structure factor S (Q, E) of Mg_3BiSb is shown in Fig. 4b, where dispersive acoustic features are observed. For the $Mg_3Bi_{2-x}Sb_x$ system, 300 K (k_BT ~ 26 meV) is sufficiently high to populate low- and mid-energy phonons and to reveal anharmonic effects. As highlighted by the black box, two acoustic phonon groups are observed: one with energy above 5.2 meV, and another, significantly flatter, around 3 meV. To further clarify the nature of the two acoustic branches, we performed a Q-integrated spectrum shown as a pink curve in Fig. 4b, which exhibits two maxima (pink arrows), one at 3 In comparison, the corresponding acoustic phonon maxima in the calculated band structures shown in Fig. 2 both lie around ~ 7.5 meV. Namely, the LA and TA modes observed in INS are considerably softer than theoretical predictions, particularly the TA mode, which achieves a dispersion maximum at only 3 meV. The softening of TA mode is attributed to the avoided-crossing effect arising from optical-acoustic phonon interaction, as observed in the triple-axis INS experiments on $Mg_3Bi_{1.5}Sb_{0.5}$.

The temperature-dependent GDOS of Mg_3BiSb was measured at 100, 150, 200, 250, and 300 K, as shown in Fig. 4c. In addition to the broadened peaks in the low- and mid-energy regions, two distinct envelope peaks corresponding to optical phonons are observed at high energies of ~ 25 meV and ~ 30 meV, respectively. These peaks exhibit progressive softening with increasing temperature, revealing anharmonic lattice vibrations associated with the Mg(2) atoms. High-energy optical phonon peaks were also observed in Mg_3Bi_2 and Mg_3Sb_2, which, based on the simulations in Fig. S6, are expected to shift to higher energies with increasing Sb concentration. Notably, in Fig. 4a, the experimental peaks of Mg_3BiSb at 300 K closely resemble those of Mg_3Bi_2 and are considerably softer than the corresponding peaks in Mg_3Sb_2. This indicats that the alloy system exhibits enhanced anharmonicity in the phonon modes dominated by Mg (1) atoms.

Discussion

The anharmonic phonon band structures, which are believed to underlie the ultralow intrinsic κ_L in $Mg_3Bi_{2-x}Sb_x$ TE materials, were thoroughly investigated using a combination of INS techniques and DFT calculations. A topological phonon crossing between the longitudinal acoustic (LA) and optical branches along the Γ - M direction was identified and precisely located. Near this crossing, the phonon peaks are significantly broadened and softened compared to DFT simulations. This crossing is expected to enhance phonon-phonon scattering by providing an enlarged scattering phase space, thereby reducing κ_L. Additionally, the transverse acoustic (TA) and optical branches exhibit “avoided-crossing” behavior along the same direction, similar to that observed in PbTe previously driven by the giant anharmonicity in lattice dynamics, which further contributes to the low κ_L. The GDOS of Mg_3BiSb, compared with those of the binary compounds Mg_3Sb_2 and Mg_3Bi_2, reveals broadened peaks in the mid- and low-energy regions, consistent with the suppression of κ_L through Bi/Sb alloying. In this work, we experimentally characterized the nontrivial topological phonons and the anharmonic avoided-crossing features in $Mg_3Bi_{2-x}Sb_x$ TE materials and elucidated the contributions of Bi/Sb alloying to the reduction of κ_L. This study provides new insights into the exceptional TE performance of this material family from the perspective of topological phonons and paves the way for the discovery of novel high-performance TE materials. Future studies incorporating energy-dependent phonon lifetimes derived from anharmonic scattering, as well as a systematic analysis of anisotropic versus isotropic lattice thermal conductivity, would be highly informative for understanding heat transport in the presence of topological phonon band crossings.

Methods

Sample preparation

Polycrystalline $Mg_{3.05}Bi_{2-x}Sb$ (x = 0, 0.5, 1, 1.5, 2) ingots were synthesized by melting stoichiometric amounts of high-purity elemental Mg (99.95%), Bi (99.99%), and Sb (99.9%) in sealed tantalum tubes in quartz ampoules at 1373 K for 6 h, quenched in cold water, and annealed at 873 K for 72 h. The tantalum tubes were sealed using an arc-melting system in argon at a pressure slightly lower than one atmosphere. An excess amount of Mg was used to compensate for the loss during synthesis because of its high vapor pressure and its causticity.

The ingots were cut into relatively large pieces (~ 3 mm in diameter) and quickly transferred to a graphite die for hot pressing.[44] Hot pressing was performed in vacuum at 773 K for 25 min under a uniaxial pressure of ~ 110 MPa using an induction heating hot-press system. Pressed pellet samples were cut into parallelepiped shape with dimensions of 1.5×3×10 mm^3 for TE properties measurements. Single-crystalline $Mg_{3.05}Bi_{1.5}$ $Sb_{0.5}$ was grown via the Bridgeman method reported in reference[38] for the triple-axis INS experiments. A photograph of the crystal is shown in Fig. S7, and the Bragg peaks of (1 0 0), (0 1 0), and (1 1 0) reflections in Fig. S8 shows good crystallization quality.

Inelastic neutron scattering experiments

Time-of-Flight inelastic neutron scattering (TOF-INS) TOF-INS measurements were performed on $Mg_{3.05}BiSb$ powder (mass ~ 8 g), which was grounded from the $Mg_{3.05}BiSb$ ingots obtained by melting mentioned in last session, using Pelican at the Australian Nuclear Science and Technology Organization (ANSTO).[45] The powder was sealed in a 25 mm diameter thin-walled aluminum can. The elastic line energy resolution was measured using a vanadium standard and verified using low-temperature samples.

For the TOF-INS measurements, we used a top-loading closed-cycle refrigerator with a hot stage. A wavelength of 4.75 Å (3.7 meV) was used for the incident neutrons, allowing energy

transfers up to 60 meV in the energy gain mode, and data were collected at 100, 150, 200, 250, and 300 K. Additionally, a wavelength of 2.345 Å (14.9 meV) was used for a larger energy range to capture the details of the low-energy phonon modes at 100 K. Empty-can background scattering data were collected in a configuration identical to that of the sample measurements.

The collected data were transformed from instrument coordinates to physical momentum transfer (*Q*) and energy transfer (*E*) using the LAMP software,[46] and the data were then normalized by the total incident neutron flux. The generalized phonon density of states (GDOS) was derived using the LAMP software.

Triple-axis inelastic neutron scattering Triple-axis INS was performed on a $Mg_{3.05}Bi_{1.5}Sb_{0.5}$ single crystal using the thermal neutron instrument Taipan and the cold neutron instrument Sika at ANSTO. Taipan was aligned with a fixed final energy of 14.87 meV and open-40'-40'-open collimation for high Q-resolution with a vertically focused monochromator to improve intensity. A graphite filter was used on the scattered arm to remove higher-order scattering. A top-loaded cryostat with a temperature range of 25 – 750 K (CF-8) was used to provide a temperature dependent sample environment. $Mg_{3.05}Bi_{1.5}Sb_{0.5}$ single crystals (~ 5 g) was mounted on an aluminium disk and aligned in the (H K 0) scattering plane to measure the longitudinal and transverse phonon modes in Γ- *M* and Γ- *K* zone (2 - 40 meV).

We used the cold neutron triple-axis spectrometer Sika to measure the same single crystal as that used in Taipan for higher-resolution energy scans. Sika was aligned with 60'-60'-60'-open collimation to provide a non-divergent beam to the sample, and the final energy was fixed at 5 meV, which resulted in an energy resolution of approximately 0.13 meV, which is an order of magnitude better than that of Taipan (0.9 meV). A cooled Be filter was used to remove higher-order contamination from the scattered beam. The $Mg_{3.05}Bi_{1.5}Sb_{0.5}$ single crystal was aligned in the same scattering plane as on Taipan. Constant *Q* energy scans were conducted on both

instruments, scanning the energy range 1 - 10 meV for Taipan and 1-8 meV for Sika. Note that, in Fig. 3, the energy of the first point near the Brillouin zone center (Γ) for each phonon branch is overestimated, which does not align with the DFT-predicted phonon dispersion. We have deleted the first data points for LA and TA that are close to zone center to avoid confusions. This systematic deviation is likely caused by the tailing effect from the strong elastic scattering (Bragg peak) at Γ, which is known to affect the fitting of low-energy phonon peaks.[47] In addition, when measuring longitudinal and transverse phonon modes, weak contributions from the opposite polarization are, in principle, expected due to the finite transverse components of the momentum transfer and the anisotropic shape of the instrumental resolution ellipsoid. However, these contributions are strongly suppressed by the scattering geometry and spectrometer acceptance and are therefore negligible compared to the dominant signal observed in our measurements.

Structure characterizations A small portion of polycrystalline Mg_3SbBi ingots were hand-ground into powders for X-ray Diffraction (XRD), and the diffraction data were collected on a DX-2007 diffractometer using Cu-Kα radiation (λ=1.15406 Å). The XRD results are shown in Fig. S9, with standard PDF#03-0375 of Mg_3Sb_2 as a reference. The microstructures were characterized using a Scanning Electron Microscope (FEI Helios 5) equipped with an energy-dispersive spectrometer (EDS) and electron backscattering diffraction. SEM results show uniformly distributed Mg, Bi, and Sb elements in the polycrystalline Mg_3SbBi sample, as shown in Fig. S10.

Thermoelectric properties measurement Polycrystalline parallelepiped-shaped specimens of Mg_3Bi_2, Mg_3Sb_2, and Mg_3BiSb with approximate dimensions 1.5×3×10 mm^3 were cut from the bulk samples. The electrical resistivity, Seebeck coefficients, and thermal conductivity were measured simultaneously using the PPMS Dynacool-12T (Quantum Design) configured with the thermal transport option (TTO) from 2 K to 300 K. This measurement was made by attaching

four leads to the sample with conducting silver epoxy. A temperature gradient was established by applying heat at one end of the specimen while holding the other end at a constant temperature by maintaining good thermal contact with a low-temperature reservoir. The temperature difference is monitored and the voltage measured at the same positions along the sample.

Theoretical modelling Density functional theory (DFT) calculations, as implemented in the Vienna ab initio Simulation Package (VASP) [48] were used to optimize the lattice structure of pristine Mg_3Bi_2 and Mg_3Sb_2, as well as three alloying structures: $Mg_3Bi_{1.5}Sb_{0.5}$, Mg_3BiSb, and $Mg_3Bi_{1.5}Sb_{0.5}$. A 1×1×2 supercell unit cell was created for the structures of $Mg_3Bi_{1.5}Sb_{0.5}$ and $Mg_3Bi_{0.5}Sb_{1.5}$. The–Perdew–Burke Ernzerhof (PBE) form of the generalized gradient approximation (GGA) was used to describe the electron exchange and correlation. [49]The kinetic energy cutoff for the plane-wave basis was set to 450 eV. We used a *Γ* - centered k-point mesh for sampling the Brillouin zone with a density of 2π×0.03 Å^(-1). The convergence of the total energy was set to 10^{-6} eV, with all forces acting on atoms being smaller than 0.01 eV/ Å.

To calculate the phonon spectrum, density functional perturbation theory (DFPT) methods, as implemented in the phonopy package[50,51], were used. A 3×3×2 supercell was created to calculate the force constants of Mg_3Bi_2, Mg_3Sb_2, and Mg_3BiSb, and a 3×3×1 supercell was created to calculate the alloying structures of $Mg_3Bi_{1.5}Sb_{0.5}$, and $Mg_3Bi_{0.5}Sb_{1.5}$. In the DFPT calculations, we used a 3×3×3 *Γ* - centered *k*-point mesh. The criteria for the convergence of the total energy were set to 10^{-8} eV. All other parameters were kept identical to those used for lattice optimization.

To recover the phonon band character in the alloyed compounds, we applied a band unfolding formalism to unfold their phonon band structures onto the Brillouin zone of the pristine unit cell.[52]

The band unfolding process led to a clearer examination of the topological phonons experimentally observed in $Mg_3Bi_{1.5}Sb_{0.5}$. To assess the topological character, we computed the Berry phase and Berry curvature around the topological phonon feature along the $\Gamma - M$.[53] We also computed the slab phonon band structure and highlighted the topologically nontrivial surface states.

Data Availability

All data supporting the findings of this study are available within the article and the Supplementary Information file. Source data in the main text are provided with this paper.

Reference

1 Zhao, W. *et al.* Quantum interference effects in a 3D topological insulator with high-temperature bulk-insulating behavior. *Applied Physics Reviews* **11** (2024).
2 Chen, L. *et al.* Topological insulator VxBi1. 08-xSn0. 02Sb0. 9Te2S as a promising n-type thermoelectric material. *Journal of Alloys and Compounds* **918**, 165550 (2022).
3 Hasan, M. Z. & Kane, C. L. Colloquium: topological insulators. *Reviews of modern physics* **82**, 3045-3067 (2010).
4 Wang, S., Lin, B.-C., Wang, A.-Q., Yu, D.-P. & Liao, Z.-M. Quantum transport in Dirac and Weyl semimetals: a review. *Advances in Physics: X* **2**, 518-544 (2017).
5 Fang, C., Chen, Y., Kee, H.-Y. & Fu, L. Topological nodal line semimetals with and without spin-orbital coupling. *Physical Review B* **92**, 081201 (2015).
6 Guo, L. *et al.* Electronic transport evidence for topological nodal-line semimetals of ZrGeSe single crystals. *ACS Applied Electronic Materials* **1**, 869-876 (2019).
7 Ren, Y., Xiao, C., Saparov, D. & Niu, Q. Phonon magnetic moment from electronic topological magnetization. *Physical review letters* **127**, 186403 (2021).
8 Saparov, D., Xiong, B., Ren, Y. & Niu, Q. Lattice dynamics with molecular Berry curvature: Chiral optical phonons. *Physical Review B* **105**, 064303 (2022).
9 Ding, Z. K., Zeng, Y. J., Liu, W., Tang, L. M. & Chen, K. Q. Topological phonons and thermoelectric conversion in crystalline materials. *Advanced Functional Materials* **34**, 2401684 (2024).
10 Xu, Y. *et al.* Catalog of topological phonon materials. *Science* **384**, eadf8458 (2024).
11 Yue, S. *et al.* Phonon softening near topological phase transitions. *Physical Review B* **102**, 235428 (2020).
12 Zhang, L., Ren, J., Wang, J.-S. & Li, B. Topological nature of the phonon Hall effect. *Physical review letters* **105**, 225901 (2010).
13 Luo, L. *et al.* Observation of a phononic higher-order Weyl semimetal. *Nature Materials* **20**, 794-799 (2021).
14 Li, J. *et al.* Computation and data driven discovery of topological phononic materials. *Nature communications* **12**, 1204 (2021).
15 Collins, J. L. *et al.* Electric-field-tuned topological phase transition in ultrathin Na3Bi. *Nature* **564**, 390-394 (2018).

16 Baydin, A. *et al.* Magnetic control of soft chiral phonons in PbTe. *Physical review letters* **128**, 075901 (2022).
17 Juraschek, D. M. *et al.* Chiral phonons. *Nature Physics* **21**, 1532-1540 (2025).
18 Miao, H. *et al.* Observation of double Weyl phonons in parity-breaking FeSi. *Physical review letters* **121**, 035302 (2018).
19 Li, J. *et al.* Direct observation of topological phonons in graphene. *Physical Review Letters* **131**, 116602 (2023).
20 Singh, S., Wu, Q., Yue, C., Romero, A. H. & Soluyanov, A. A. Topological phonons and thermoelectricity in triple-point metals. *Physical Review Materials* **2**, 114204 (2018).
21 Zhang, J. *et al.* Anomalous thermoelectric effects of ZrTe 5 in and beyond the quantum limit. *Physical review letters* **123**, 196602 (2019).
22 Hooda, M. & Yadav, C. Enhanced thermopower and low thermal conductivity in p-type polycrystalline ZrTe5. *Applied Physics Letters* **111** (2017).
23 Hong, M. *et al.* Computer-aided design of high-efficiency GeTe-based thermoelectric devices. *Energy Environmental Science* **13**, 1856-1864 (2020).
24 Chen, W. *et al.* Nanobinders advance screen-printed flexible thermoelectrics. *Science* **386**, 1265-1271 (2024).
25 Hong, M., Lyu, W., Wang, Y., Zou, J. & Chen, Z.-G. Establishing the golden range of Seebeck coefficient for maximizing thermoelectric performance. *Journal of the American Chemical Society* **142**, 2672-2681 (2020).
26 Delaire, O. *et al.* Giant anharmonic phonon scattering in PbTe. *Nature materials* **10**, 614-619 (2011).
27 Li, C. W. *et al.* Orbitally driven giant phonon anharmonicity in SnSe. *Nature Physics* **11**, 1063-1069 (2015).
28 Zhang, Y. *et al.* Realizing high power factor and thermoelectric performance in band engineered AgSbTe2. *Nature communications* **16**, 22 (2025).
29 Ma, J. *et al.* Glass-like phonon scattering from a spontaneous nanostructure in AgSbTe2. *Nature nanotechnology* **8**, 445-451 (2013).
30 Ren, Q. *et al.* Extreme phonon anharmonicity underpins superionic diffusion and ultralow thermal conductivity in argyrodite Ag8SnSe6. *Nature materials* **22**, 999-1006 (2023).
31 Bano, S., Chetty, R., Babu, J. & Mori, T. Mg3 (Sb, Bi) 2-based materials and devices rivaling bismuth telluride for thermoelectric power generation and cooling. *Device* **2** (2024).
32 Jin, M., Lin, S., Li, W., Zhang, X. & Pei, Y. Nearly isotropic transport properties in anisotropically structured n-type single-crystalline Mg3Sb2. *Materials Today Physics* **21**, 100508 (2021).
33 Shi, X. *et al.* Extraordinary n-type Mg3SbBi thermoelectrics enabled by Yttrium doping. *Advanced Materials* **31**, 1903387 (2019).
34 Hong, M., Li, M., Wang, Y., Shi, X. L. & Chen, Z. G. Advances in versatile GeTe thermoelectrics from materials to devices. *Advanced Materials* **35**, 2208272 (2023).
35 Hong, M. & Chen, Z.-G. Chemistry in advancing thermoelectric GeTe materials. *Accounts of Chemical Research* **55**, 3178-3190 (2022).
36 Peng, W., Petretto, G., Rignanese, G.-M., Hautier, G. & Zevalkink, A. An unlikely route to low lattice thermal conductivity: small atoms in a simple layered structure. *Joule* **2**, 1879-1893 (2018).
37 Ding, J. *et al.* Soft anharmonic phonons and ultralow thermal conductivity in Mg3 (Sb, Bi) 2 thermoelectrics. *Science advances* **7**, eabg1449 (2021).
38 Wang, Q.-Q. *et al.* High thermoelectric performance and anisotropy studies of n-type Mg3Bi2-based single crystal. *Acta Materialia* **255**, 119028 (2023).
39 Hung, N. T. The role of spin–orbit interaction in low thermal conductivity of Mg3Bi2. *Applied Physics Letters* **123** (2023).
40 Kim, H.-S., Gibbs, Z. M., Tang, Y., Wang, H. & Snyder, G. J. Characterization of Lorenz number with Seebeck coefficient measurement. *APL materials* **3** (2015).
41 Wang, L., Li, A., Wu, X., Li, J. & Mori, T. Leveraging carrier mobility enables high-performance Mg3 (Sb, Bi) 2 thermoelectrics. *National Science Review* **13**, nwaf507 (2026).

42 Kanno, T. *et al.* High-density Frenkel defects as origin of n-type thermoelectric performance and low thermal conductivity in Mg3Sb2-based materials. *Advanced Functional Materials* **31**, 2008469 (2021).

43 Feng, Q., He, J., Wang, W. & Liu, H. Low Thermal Conductivity in Single Crystalline Mg3Bi2 and Its Thermopower Enhanced by Electron-Phonon Interaction. *Advanced Science* **12**, 2416518 (2025).

44 Shi, X. *et al.* Revelation of inherently high mobility enables Mg3Sb2 as a sustainable alternative to n-Bi2Te3 thermoelectrics. *Advanced science* **6**, 1802286 (2019).

45 Yu, D., Mole, R., Noakes, T., Kennedy, S. & Robinson, R. Pelican—a time of flight cold neutron polarization analysis spectrometer at OPAL. *Journal of the Physical Society of Japan* **82**, SA027 (2013).

46 Richard, D., Ferrand, M. & Kearley, G. Analysis and visualisation of neutron-scattering data. *Journal of Neutron Research* **4**, 33-39 (1996).

47 Shirane, G., Shapiro, S. M. & Tranquada, J. M. *Neutron scattering with a triple-axis spectrometer: basic techniques*. (Cambridge University Press, 2002).

48 Kresse, G. & Furthmüller, J. Efficiency of ab-initio total energy calculations for metals and semiconductors using a plane-wave basis set. *Computational materials science* **6**, 15-50 (1996).

49 Perdew, J. P., Burke, K. & Ernzerhof, M. Generalized gradient approximation made simple. *Physical review letters* **77**, 3865 (1996).

50 Togo, A., Chaput, L., Tadano, T. & Tanaka, I. Implementation strategies in phonopy and phono3py. *Journal of Physics: Condensed Matter* **35**, 353001 (2023).

51 Togo, A. First-principles phonon calculations with phonopy and phono3py. *Journal of the Physical Society of Japan* **92**, 012001 (2023).

52 Allen, P. B., Berlijn, T., Casavant, D. & Soler, J. Recovering hidden Bloch character: Unfolding electrons, phonons, and slabs. *Physical Review B-Condensed Matter Materials Physics* **87**, 085322 (2013).

53 Li, J. *et al.* Topological phonons in graphene. *Physical Review B* **101**, 081403 (2020).

Acknowledgement

We thank ANSTO for the allocation of neutron beam time on Taipan (P16832), Sika (P16828), and Pelican (P15920). L.C. acknowledges the support and mentoring from Prof. Yanzhong Pei at Tongji University, and the support from AINSE through ECRG funding. M.H. and L.C. acknowledge the iLAuNCH Trailblazer, Department of Education, Australia. The authors acknowledge the funding from the Australian Research Council: FT230100316 (M.H.) and IH200100035 (M.H.). The authors acknowledge the use of the instruments and scientific and technical assistance at the Monash Centre for Electron Microscopy, Monash University, a Microscopy Australia (ROR: 042mm0k03) facility supported by NCRIS. This research used equipment funded by Australian Research Council grants (LE 200100132). We also acknowledge the computational support from the National Computational Infrastructure (NCI Australia), an NCRIS enabled capability supported by the Australian Government.

Author Contributions Statement

L.C. conceived this idea. M.H., S.X. and W.Z. supervised this project. S.Z., X.Z., Z.C., S.L. and S.X. prepared the samples. L.C. conducted the experiments and data analyses. Y.Y. conducted the DFT calculations. R.A.M., D.Y. and K.C.R. helped with the inelastic neutron scattering experiments. T.L., H.M., S.H., P.S., J.B., and J.K. contributed to the discussion. L.C., Y.Y. wrote the first manuscript. All authors joined the manuscript revision.

Competing Interest Statement

The authors declare no competing interests.

Fig. 1 Topological phonons in $Mg_3Bi_{2-x}Sb_x$ compounds.

(a) Crystal structure of $Mg_3Bi_{2-x}Sb_x$ compounds. (b) The 3D view of topological phonon band crossing points near the Γ - *M* high-symmetry line (black dot). (c) Schematic of typical three-phonon scattering processing in bulk materials where ω is the energy and *q* is the momentum of the phonon. (d) The two allowed acoustic-optical phonon interactions in Γ - *M* zone, namely, the topological phonon and avoided-crossing phonon. The star symbols represent the measured results from the INS, which will be discussed in detail later.

Fig. 2 The phonon band structures from DFT calculations.

(a) Schematic of the first BZ with high-symmetry points labelled in $Mg_3Bi_{2-x}Sb_x$. Calculated phonon band structures of $Mg_3Bi_{2-x}Sb_x$ compounds. (b-f) In-basal-plane phonon spectra of different compounds, where the color code shows absolute values of the mode Gruneisen parameter of each phonon band. For $Mg_3Bi_{1.5}Sb_{0.5}$ and $Mg_3Bi_{0.5}Sb_{1.5,}$ the phonon bands unfolded into the five-atom primitive cell of Mg_3X_2 (*X*=Bi, Sb). The transparency of the bands represents the unfolding weight of phononic bands. A comparison of the unfolded and folded band structures of $Mg_3Bi_{1.5}Sb_{0.5}$ is shown in Fig. S 12. The purple and orange boxes in (d) and (e) represent the triple-axis INS and TOF-INS experimental areas, respectively.

Fig. 3 The topological phonon measurements.

The inelastic neutron scattering experiments measured using constant *Q* scans in (a, b) Γ - *M*, and (c, d) Γ - *K* zones at 100 K. Specifically, the spectra at certain *Q* points are plotted in zoom-in view (2 or 3 times on intensity), the relative intensity scale is indicated with $\times$2 or $\times$3. The blue and green stars under the peaks in (a) refers to the corresponding LA and optical phonon, and the large gradient stars refers to the TP crossing. (e, f) Longitudinal and transverse phonon (blue

stars: acoustic phonons, red circles: optical phonons) locations and linewidth extracted from peaks in (a, b, c, d) in Γ - *M*, Γ - *K* zones at 100 K. The data of the light blue star near zone center in (f) is from Sika in Fig. S5. The solid lines represent the calculated phonon dispersion. The linewidth of each measured phonon peak is plotted on the top of (e) and (f) as dropped lines. The DFT simulated LA and optical branches in (e) that topologically crossed, and the TA and TO branches in (f) that avoided crossing are marked with green and pink highlight lines.

Fig. 4 Anharmonicity of Mg_3BiSb phonons.

(a) Room-temperature phonon GDOS from INS of Mg_3BiSb (this work), Mg_3Sb_2,[37] and Mg_3Bi_2.[37] (b) Powder-averaged lattice dynamical structure factor *S* (*Q, E*) of Mg_3BiSb measured at 300 K in energy-loss mode with 14.9 meV incident neutron energy. The pink line is a *Q* - integrated spectrum, which uses the energy transfer axis as *x* and an arbitrary unit along the *y*-axis with higher intensity on the right side. (c) Temperature-dependent GDOS spectra of Mg_3BiSb are shown in the stacking mode from 100 to 300 K, where the DFT simulation results are shown in the grey box. High-energy optical phonons are enclosed in two envelope peaks, as indicated by the arrows. (d) Temperature-dependent envelope peak positions fitted by linear lines, in which the error bar is obtained from the fitting.

Editorial Summary

Authors reveal symmetry-protected topological phonons and strong phonon interactions in the thermoelectric $Mg_3Bi_{2-x}Sb_x$ family, explaining its low thermal conductivity and offering a strategy to engineer heat flow in thermoelectric materials.

Peer review information: *Nature Communications* thanks Fabian Garmroudi, Tribhuwan Pandey, Qiyang Sun and the other anonymous reviewer(s) for their contribution to the peer review of this work. A peer review file is available.

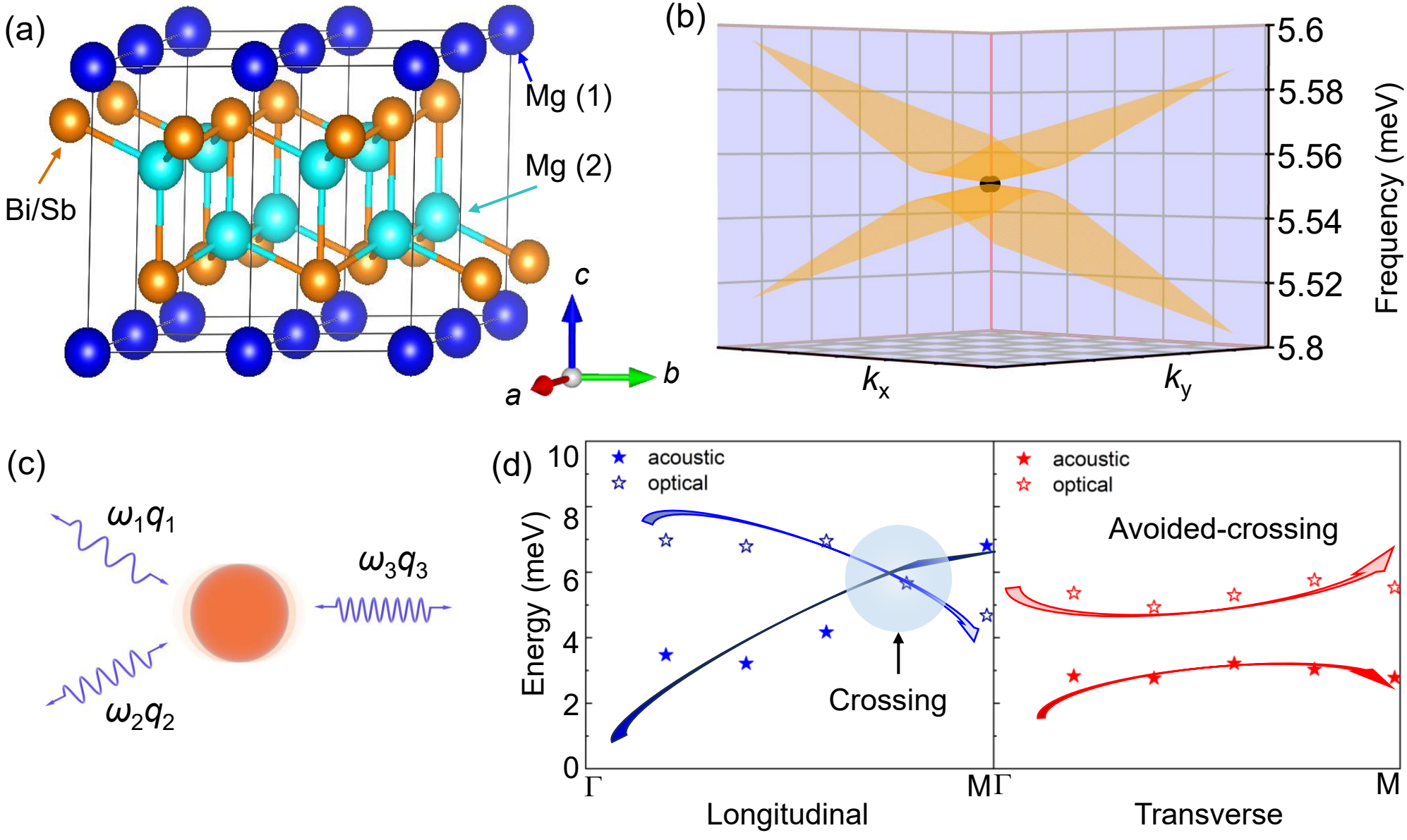
(a)
Mg (1)
Mg (2)
Bi/Sb
c
b
a
(b)
5.6
5.58
5.56
5.54
5.52
5.8
Frequency (meV)
k_x
k_y
(c)
$\omega_1 q_1$
$\omega_3 q_3$
$\omega_2 q_2$
(d)
acoustic
optical
Energy (meV)
10
8
6
4
2
0
Crossing
Γ
M
Longitudinal
acoustic
optical
Avoided-crossing
Γ
M
Transverse

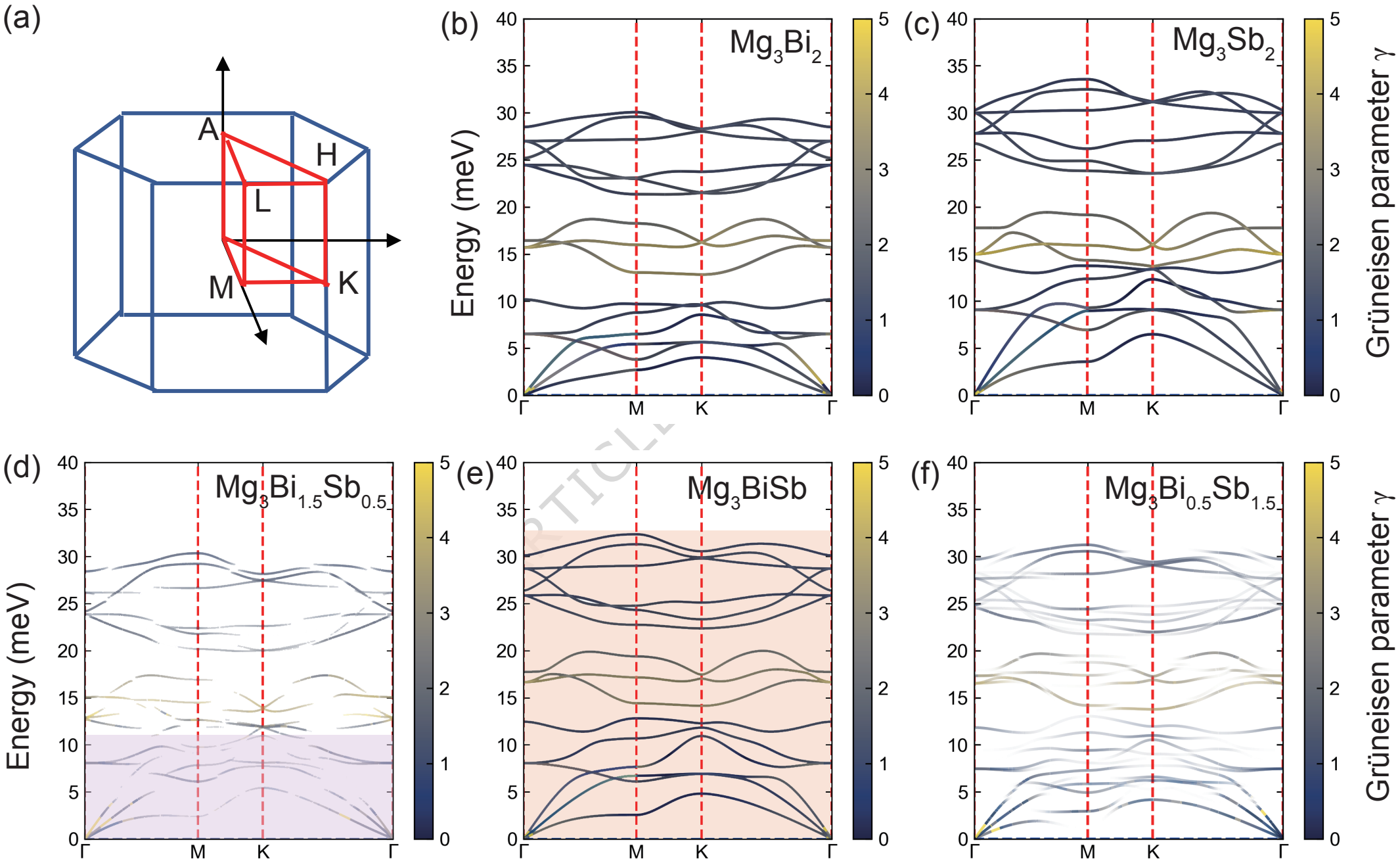
(a)
A
H
L
M
K
(b)
Mg_3Bi_2
Energy (meV)
Γ
M
K
Γ
(c)
Mg_3Sb_2
Grüneisen parameter γ
(d)
$Mg_3Bi_{1.5}Sb_{0.5}$
(e)
Mg_3BiSb
(f)
$Mg_3Bi_{0.5}Sb_{1.5}$

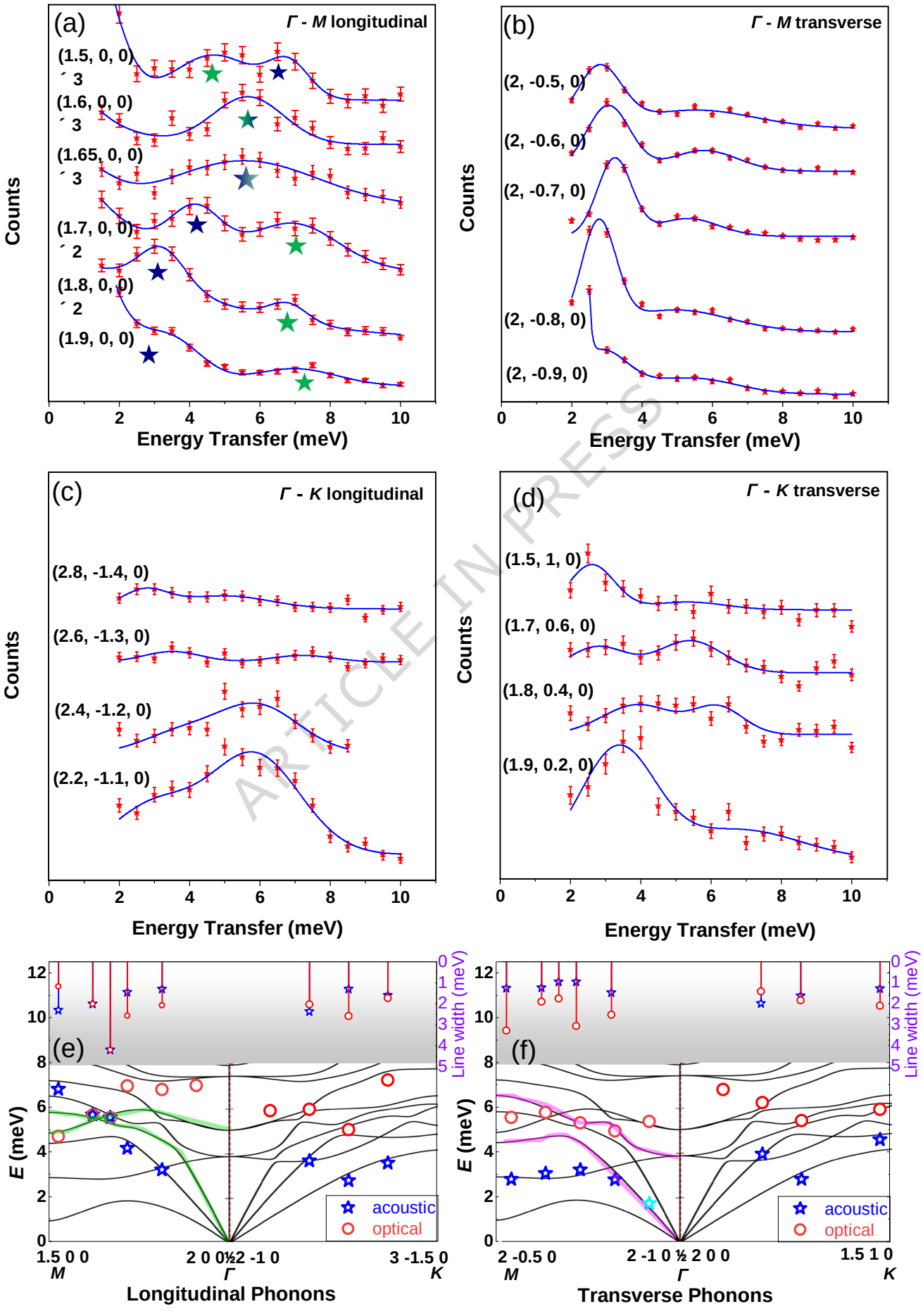

(a)

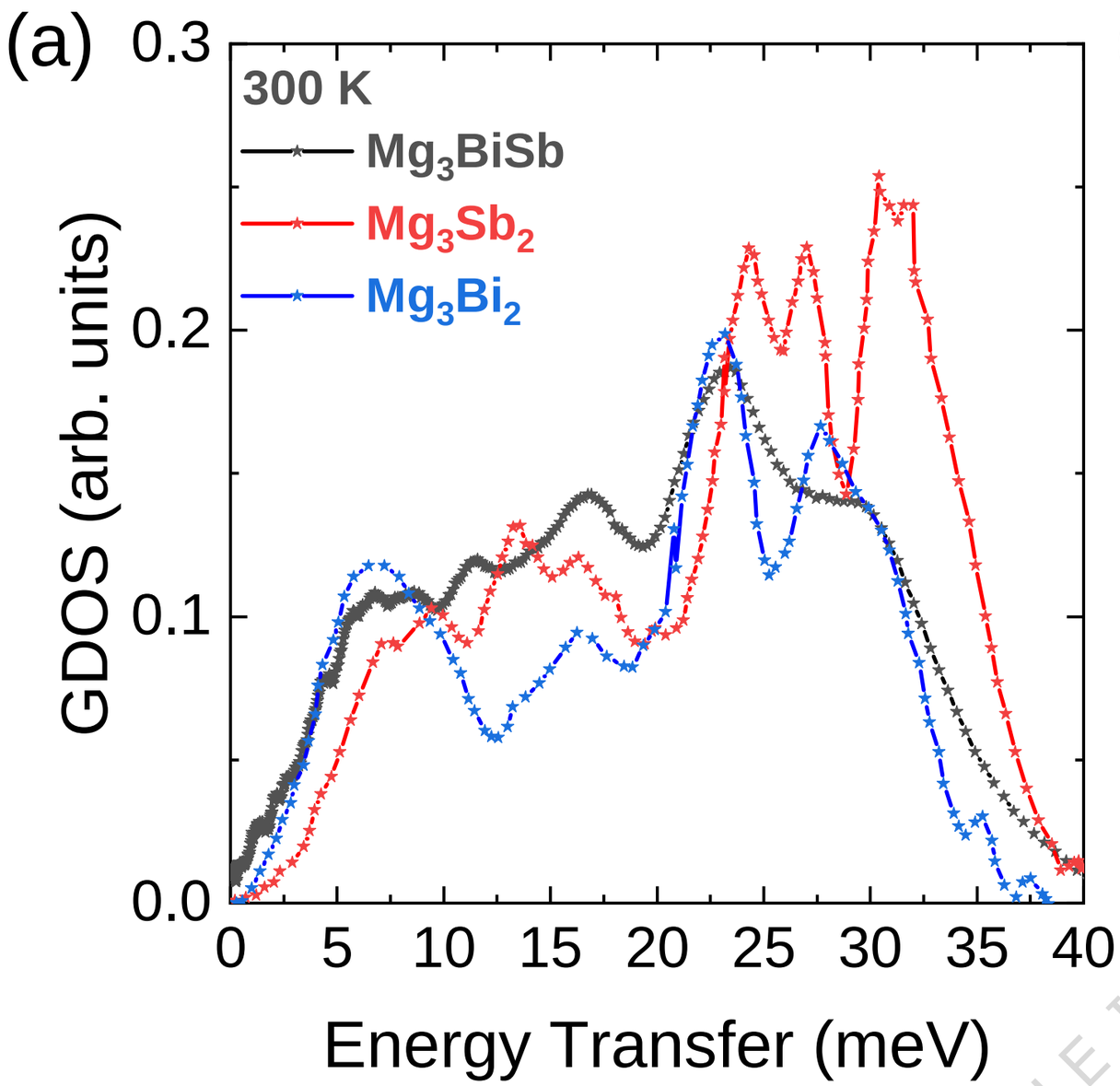
300 K
Mg3BiSb
Mg3Sb2
Mg3Bi2
GDOS (arb. units)
0.0
0.1
0.2
0.3
0
5
10
15
20
25
30
35
40
Energy Transfer (meV)

(b)

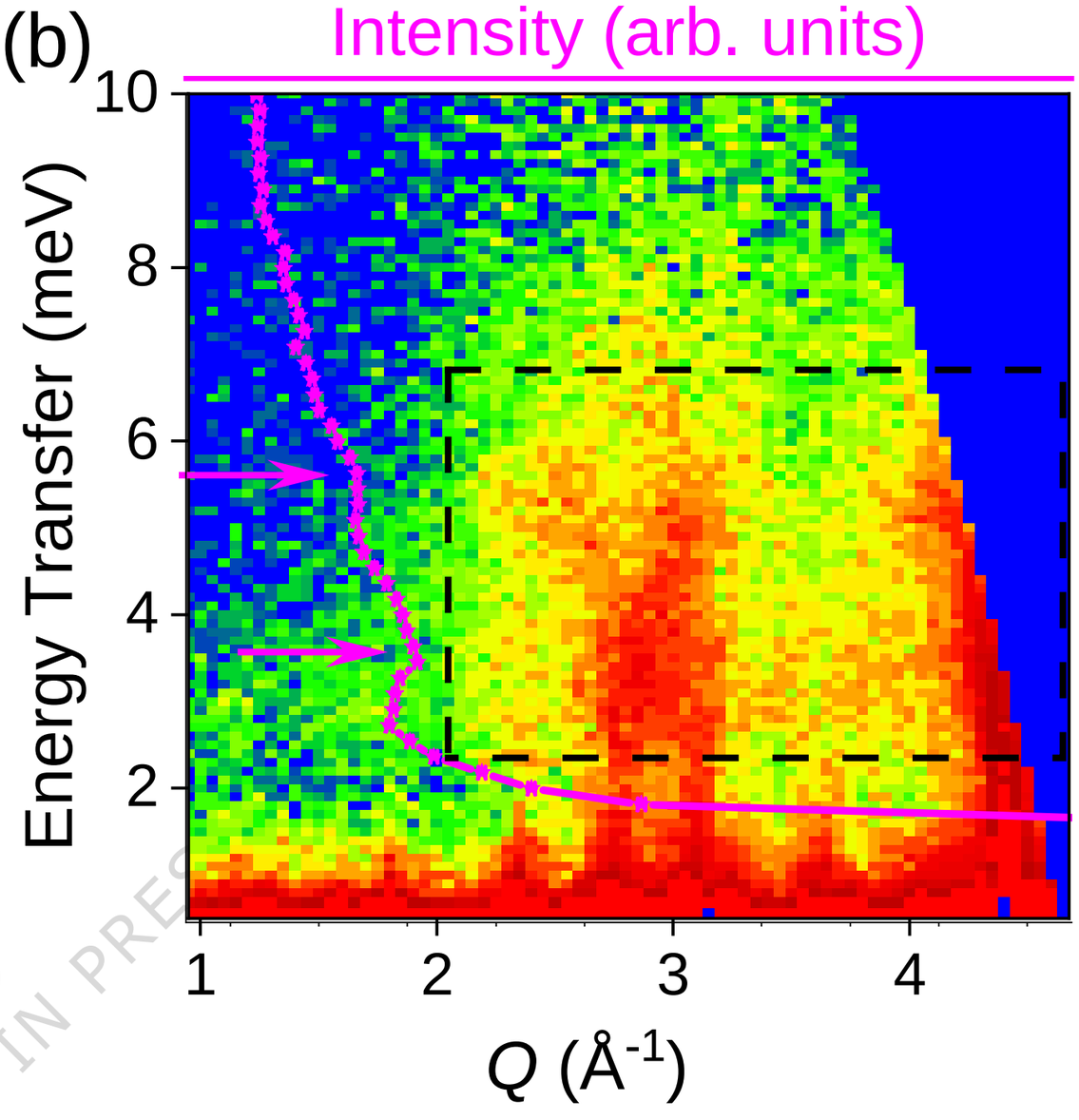
Intensity (arb. units)
Energy Transfer (meV)
2
4
6
8
10
1
2
3
4
Q (Å-1)

(c)

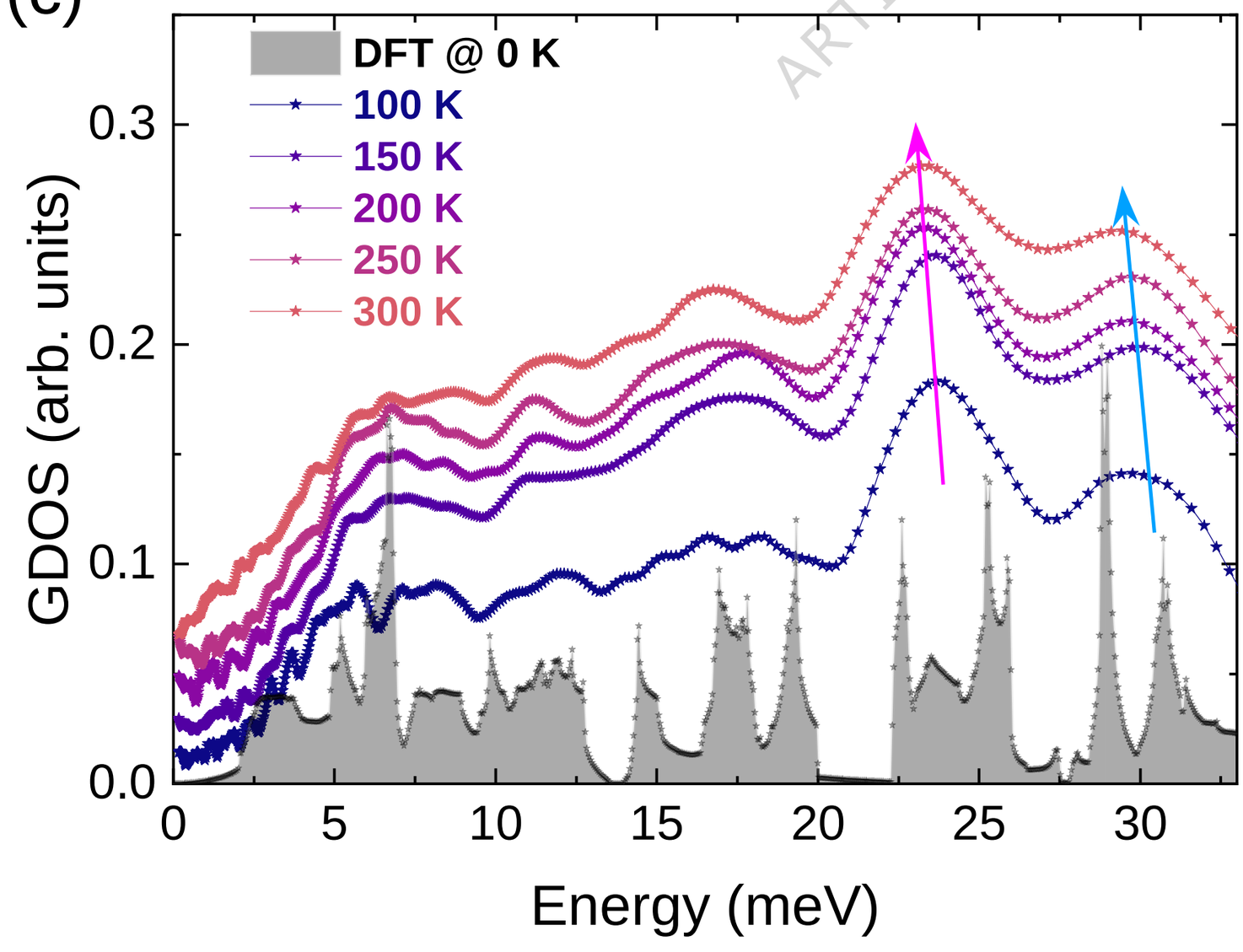
DFT @ 0 K
100 K
150 K
200 K
250 K
300 K
GDOS (arb. units)
0.0
0.1
0.2
0.3
0
5
10
15
20
25
30
Energy (meV)

(d)

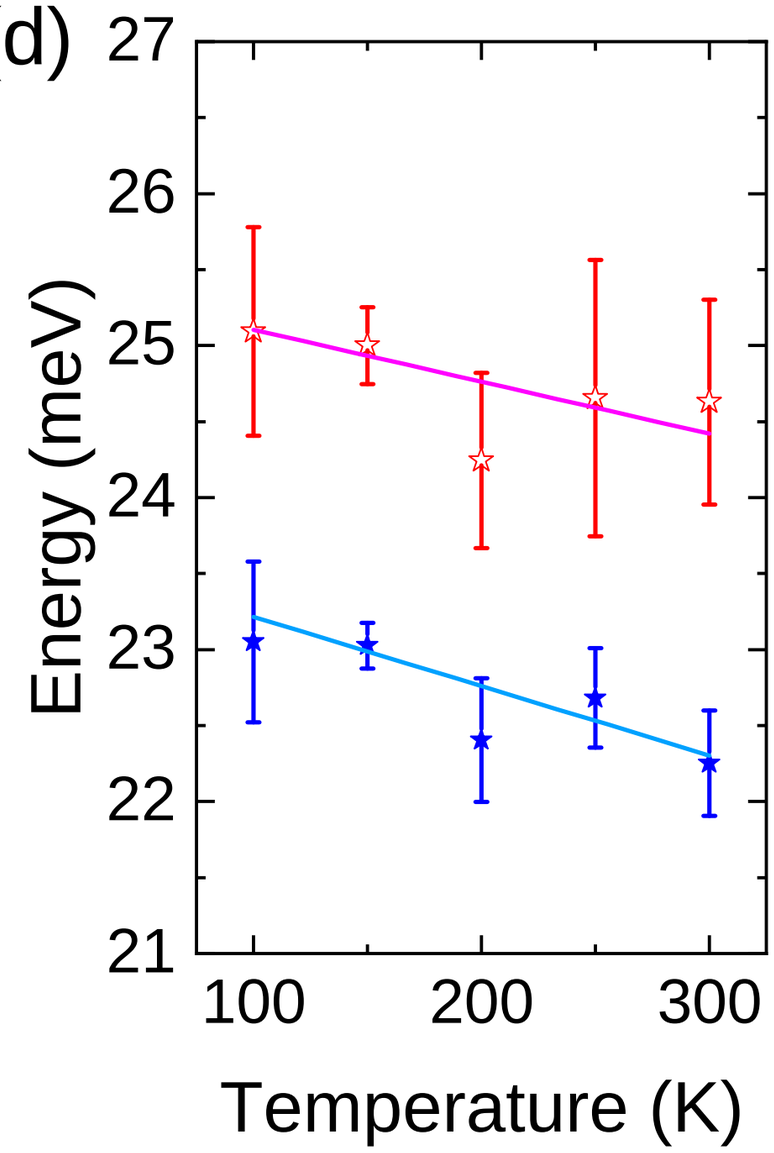
Energy (meV)
21
22
23
24
25
26
27
100
200
300
Temperature (K)